J. Adhesion Sci. Technol., Vol. 20, No. 4, pp. 277–305 (2006)
© VSP 2006.
Also available online - www.vsppub.com

Fracture behavior of an epoxy/aluminum interface reinforced by sol–gel coatings

JIONG LIU [1], MANOJ K. CHAUDHURY [1,*], DOUGLAS H. BERRY [2], JILL E. SEEBERGH [2], JOSEPH H. OSBORNE [2] and KAY Y. BLOHOWIAK [2]

[1] *Department of Chemical Engineering, Lehigh University, Bethlehem, PA 18015, USA*
[2] *The Boeing Company, P.O. Box 3707, Seattle, WA 98124, USA*

Received in final form 15 January 2006

Abstract—The strengths of epoxy/aluminum joints reinforced with a zirconium-silicon based sol–gel adhesion promoter were investigated using an ADCB (Asymmetric Double Cantilever Beam) wedge test. The fracture energies and loci of failure of these joints were shown to depend upon the mixity of the normal and shear modes of stress acting at the crack. The ADCB geometry enabled the crack to propagate along the epoxy/aluminum interfaces so that the effect of surface pretreatment and the processing conditions of the adhesion promoter on adhesion strength could be directly evaluated. The dry strength of these joints depends on the thickness of the sol–gel film derived from different concentrations of the precursors. Thinner films are more fully crosslinked and thus give higher adhesion strengths than those obtained with thicker films. The differences in the wet strengths of the sol–gel reinforced joints for various surface pretreatments suggest that the sol–gel films are subject to moisture degradation with certain surface pretreatments. The loci of failure of many of these joints alternate between the sol–gel/aluminum and epoxy/sol–gel interfaces. This behavior is similar to that observed more generally in adhesively-bonded joints tested in DCB (Double Cantilever Beam) geometry. The brittle *versus* ductile behavior associated with the failure process reveals important information about how the sol–gel films affect the adhesion strength.

Keywords: ADCB wedge test; epoxy/aluminum joints; fracture behavior; sol–gel coating.

1. INTRODUCTION

A frequently encountered problem in the performance of a polymer/metal joint is that its properties deteriorate upon exposure to aggressive service environments. The adhesion of the polymer/metal interface usually results from molecular interactions (Lewis acid–base, dispersion, hydrogen bonding, etc.), as well as mechanical

*To whom correspondence should be addressed. Tel.: (1-610) 758-4471. Fax: (1-610) 758-5057. E-mail: mkc4@lehigh.edu

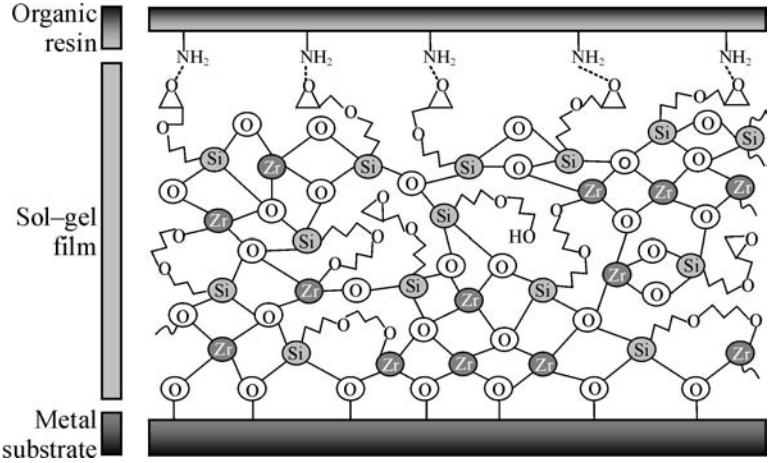

Figure 1. Schematic of a sol–gel adhesion promoting coating. The sol–gel film (typically 50–200 nm) is derived from the condensation reactions of a sol prepared from a mixture of glycidoxy functional silane and zirconium alkoxide. An inorganic/organic gradient is created to achieve good adhesion. XPS study indicates that the interface near the metal substrate is zirconium-rich and the top film surface is silane-rich [13].

interlocking, all of which depend on the substrate pretreatment conditions [1]. Considerable progress [2–5] has been made in reinforcing the polymer/metal joint with organofunctional silanes that promote covalent bonding throughout the interface, thus providing improved bond durability. Recently, a sol–gel process was developed at Boeing [6–13] which has shown improved performance over the silane-only process. As shown in Fig. 1, thin films are produced onto metal substrates from dilute aqueous solutions of a silane coupling agent and zirconium alkoxide precursor, both of which are hydrolyzed to hydroxides and react with the hydroxyl groups on the metal surface *via* condensation. The organic functional groups of the silanes are chosen such that they react with the polymeric resin; for instance, the glycidoxy functionality of the coupling agent will react with the amine groups of the epoxy resins. In between the polymer and metal, a hybrid organic/inorganic coating is formed through the self-condensation crosslinking process. The bonded system provides strong adhesion protection in aggressive environments.

The improved performance of the sol–gel process as compared with the silane-only process in hot/wet conditioning is possibly due to the incorporation of the zirconium alkoxide. The zirconium alkoxide catalyzes the condensation reaction during the crosslinking process [14], thus making the room temperature drying of the film possible. The zirconium moiety also functions as an oxygen diffusion barrier [9–12, 15], thus improving the corrosion resistance of the joint. Although the sol–gel chemistry is versatile, the cross-linking process is highly dependent on processing conditions [14]. To date, no thorough studies have been carried out to elucidate the adhesion-promoting mechanisms of the sol–gel-derived conversion coatings. Another issue of particular interest is how the pretreatment affects

the adhesion strength and durability of a joint. Work done by Blohowiak and co-workers [7, 16] and McCray and co-workers [17, 18] demonstrated a large difference in hot/wet performance of the sol–gel coatings in the peel and DCB (Double Cantilever Beam) wedge tests. While valuable information has been obtained from these tests, a common problem is that the failure modes are usually not truly interfacial because the large modulus mismatch across the bi-material interface often causes cohesive failure of the polymer. This leads to difficulty in interpreting the measured fracture energy data.

The current work uses a wedge test in conjunction with the widely used ADCB (Asymmetric Double Cantilever Beam) specimen [19–23] to measure the fracture energy of the sol–gel reinforced epoxy/aluminum joint. By selecting an appropriate specimen geometry, the wedge test can force the crack to propagate along the epoxy/aluminum interface. The study starts with the measurement of the fracture energy as a function of the thickness ratio of the epoxy and aluminum beams in order to identify the conditions for minimum fracture energy. Using the parameters found from these measurements, the effects of the substrate pretreatment and sol–gel concentration are investigated under both dry and wet conditions. X-ray photoelectron spectroscopy (XPS) and scanning electron microscopy (SEM) are used to identify the locus of failure.

2. EXPERIMENTAL

2.1. Materials

Bare 2024-T3 aluminum alloy (supplied by Boeing, Seattle, WA, USA) was used as the substrate. The bulk chemical composition of this alloy is given in Table 1. The room temperature curable epoxy system used in this study was based on diglycidyl ether of bisphenol-A (DGEBA) with an epoxide equivalent weight of 187.5 (EPON 828, Resolution Performance Products, Houston, TX, USA). The curing agent was aminoethyl piperazine (EPICURE 3200, Air Products and Chemicals, Allentown, PA, USA). Five parts of carboxyl-terminated butadiene acrylonitrile (Hycar CTBN 1300X8, Noveon, Cleveland, OH, USA) per hundred parts of DGEBA were used as toughener. CTBN was pre-reacted with the epoxy resin by mixing them at 140°C for 4 h to make an adduct. The resin adduct and curing agent were mixed thoroughly using the stoichiometric ratio and degassed by centrifugation. After applying onto the sol–gel-treated substrates, the resin was post-cured according to the following protocol. The specimen was ramped from room temperature to 100°C in 4 h,

Table 1.
Chemical composition of bare 2024-T3 aluminum alloy (wt%)*

Si	Fe	Cu	Mn	Mg	Cr	Zn	Ti	Al
0.5	0.5	3.8–4.9	0.3–0.9	1.2–1.8	0.1	0.25	0.15	remainder

*From ASTM B 209-01.

held at 100°C for 2 h, and then cooled down to room temperature in 6 h. The heating and cooling processes were programmed using a temperature controller. This cure procedure minimizes the residual thermal stress in the cured samples. The fracture behavior and toughening mechanisms for the bulk material of the present epoxy system were studied by Bagheri and Pearson [24, 25]. The glass transition temperature of this epoxy was measured by differential scanning calorimetry to be 105°C.

The sol–gel solutions were prepared following the procedures described in the literature for Boegel EPII [6–12, 26]. GPTMS (glycidoxypropyltrimethoxysilane) (97%, Gelest, Morrisville, PA, USA), TPOZ (zirconium tetrapropoxide) (68–70%, Strem Chemicals, Newburyport, MA, USA), glacial acetic acid (Aldrich, St. Louis, MO, USA) and Antarox BL-240 (Rhodia, Cranbury, NJ, USA) were used as-received. Sol–gel solutions of different concentrations were formulated by adding different amounts of water to a standard stock solution. The sol–gel concentration reported here is the volume concentration of GPTMS and TPOZ combined. The resultant sol–gel solution was then applied to the substrates within 2 h.

2.2. Surface pretreatment

The as-received 2024-T3 aluminum alloy of 1.016 mm thickness was cut into 12.7 mm × 50.8 mm coupons. The substrates were then solvent wiped with methyl ethyl ketone and acetone followed by alkaline cleaning using Isoprep 44 (MacDermid, Waterbury, CT, USA) solution at 60°C for 10 min (Boeing Process Specification BAC5749), rinsed with water and allowed to dry at room temperature. The samples were then subjected to various deoxidation methods to create different surface morphologies and topographies on the substrates prior to the sol–gel application.

The first method involved polishing, where the substrates were ground mechanically with 600 grit silicon carbide paper, polished with 6 μm and 1 μm diamond pastes, and then alkaline cleaned one more time and flame-treated quickly using a propane torch just prior to the sol–gel application. (The sol–gel solution sometimes did not wet the as-polished substrate, indicating that contaminants were adsorbed. A similar observation was made by Dillingham and Boerio [27]. The flame treatment made the polished substrate consistently wettable by sol–gel.) This pretreatment produced a mirror-like flat surface and kept the hydrocarbon contamination to a minimum.

The second method involved chemical etching, in which the substrates were immersed in FPL (Forest Products Laboratory) solution [28] at 68°C for 10 min. This pretreatment produced a highly reproducible surface with micro-rough features (Venables [28] defined a micro-rough surface as having a fine structure with dimensions 0.1 μm or less).

The third method was sanding with 180 mesh alumina grit (Merit Abrasives, Garden Grove, CA, USA) sandpaper using a random orbital sander. This particular

Table 2.
XPS elemental percentage data (at%) for pretreated surfaces before sol–gel application

	Al	O	C	Cu	Si	Mg	Na	N	S
Polished	27.8	49.2	21.9	0.5	0.2	0.2		0.2	
FPL etched	28.6	47.9	22.7	0.3	0.5				
Sanded	32.6	41.4	23.2	0.2	0.1	1.6		0.9	
Grit-blasted	20.3	40.7	31.3	0.1	1.6	1.2	3.1		1.6

sandpaper was found to leave a clean, uncontaminated surface in prior Boeing studies [16].

The fourth method was grit-blasting, in which the substrates were blasted with 50 μm alumina grit fluidized in pressurized (4.1 atm) air.

The last two pretreatments (sanding and grit-blasting) produced macroscopically rough surfaces as shown in Figs 15B and 17B, respectively. The elemental percentage data measured by XPS for the above pretreated surfaces are listed in Table 2.

2.3. Sol–gel application

Within 1 h after the pretreatments, the pretreated substrates were wetted by sol–gel solutions for 2 min, spun at 800 rpm for 50 s and then allowed to dry under different conditions. This application method produced a uniform film and improved the repeatability of the measurements. In the present study, the sol–gel films were all dried at room temperature for 3 h, except where noted.

2.4. Specimen preparation

The ADCB specimen (Fig. 2) was prepared using the following procedure (Fig. 3). After sol–gel application, a thin film of poly(tetrafluoroethylene) (PTFE) was sprayed at each end of the substrate to serve as the pre-crack, after which the aluminum substrate was held in place at the bottom of a silicone rubber mold, the width and length of which were exactly the same as those of the substrate. The uncured epoxy was then poured onto the substrate and a glass slide bearing a thin PTFE film was placed on the top to squeeze out the extra epoxy. The thickness of the epoxy slab was controlled by the height of the mold. After the complete cure of the epoxy, the cover glass was detached and extra epoxy was cut off.

2.5. Fracture energy measurement

The fracture energy of the joint was evaluated by measuring the critical strain energy release rate, G, of the crack. For the ADCB specimen (Fig. 2), the energy release rate can be calculated using Kanninen's model of beams on elastic foundation [29], which has been validated by both boundary element and finite element analyses

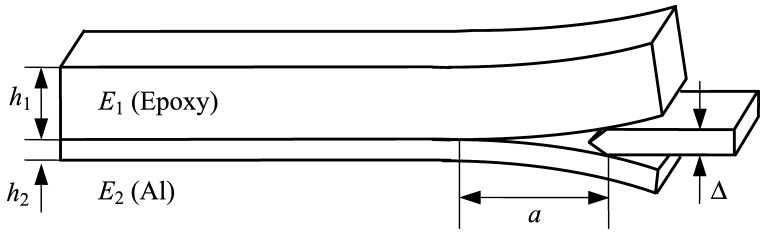

Figure 2. Schematic of the ADCB specimen. The strain energy release rate for this specimen is a function of the crack length a, wedge thickness Δ and materials constants E_1, E_2, h_1 and h_2, where E_1 and E_2 are the elastic moduli of epoxy and aluminum beams, respectively, while h_1 and h_2 stand for the thicknesses of the epoxy and aluminum beams, respectively.

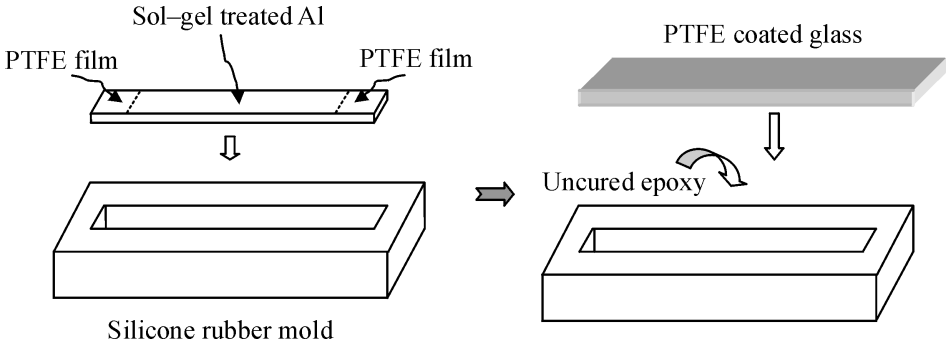

Figure 3. Schematic of the procedure for fabricating the ADCB specimen. The sol–gel-treated and pre-cracked aluminum substrate is inserted into the silicone rubber mold to be held in place. The mold is then filled with uncured epoxy. Finally, a PTFE-coated glass slide is placed on top to squeeze out the extra epoxy.

[30, 31]. G is given by:

$$G = \frac{3\Delta^2 E_1 h_1^3 E_2 h_2^3}{8a^4}\left[\frac{E_1 h_1^3 C_2^2 + E_2 h_2^3 C_1^2}{(E_1 h_1^3 C_2^3 + E_2 h_2^3 C_1^3)^2}\right], \tag{1}$$

where $C_1 = 1 + 0.64h_1/a$, $C_2 = 1 + 0.64h_2/a$, Δ is the wedge thickness, E is the elastic modulus, h is the beam thickness, a is the crack length, and subscripts 1 and 2 refer to epoxy beam and aluminum beam, respectively.

The energy release rate given by the above equation assumes that the ADCB specimen is free of pre-stress. However, in the present system, there is a large mismatch in the thermal expansion coefficient between the epoxy and aluminum (Table 3), suggesting that a residual thermal stress develops in the specimen. As a result, the specimen becomes slightly warped when cooled from cure temperature to room temperature. This affects the energy release rate calculation in equation (1). A simple analysis (see Appendix) shows that the energy release rate due to thermal loading (G_T) for an ADCB specimen can be calculated analytically. It turns out that the thermal stress has little effect in the present study (see Appendix), and therefore was neglected.

Table 3.
Mechanical and thermal properties of 2024-T3 aluminum and model toughened epoxy

Material	Elastic modulus (E, GPa)	Poisson's ratio (ν)	Coefficient of thermal expansion (α, ppm/°C)
Bare 2024-T3	72.4	0.33	22.9
Model toughened epoxy	2.8	0.38	65*

The elastic modulus of the epoxy was measured using a dynamic mechanical analyzer (DMA) operating in torsion mode with the assumption that Poisson's ratio $\nu = 0.38$. The data for 2024-T3 were obtained from Ref. [32].

*From Ref. [33].

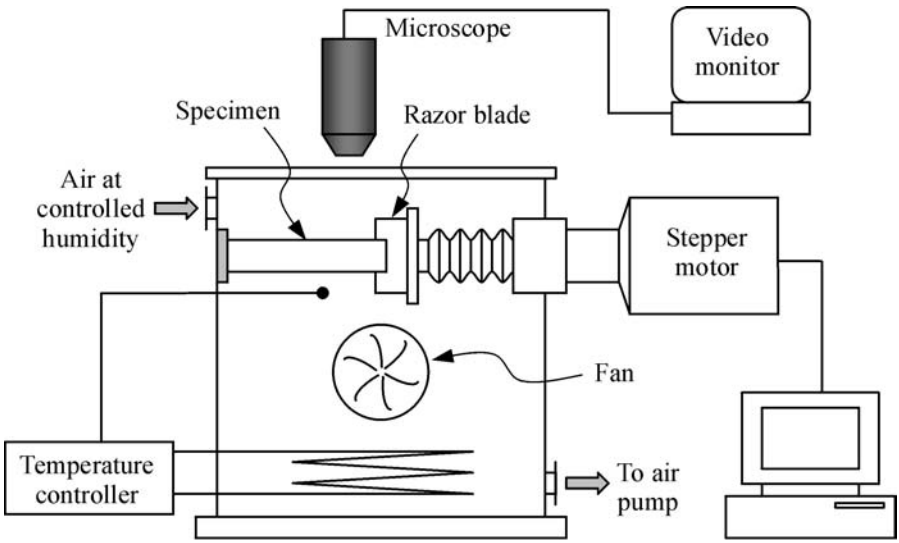

Figure 4. Schematic of the ADCB wedge test setup. The specimen is fixed in an environmental chamber (150 mm × 140 mm × 120 mm) where the temperature and humidity are well-controlled. The measurements can be conducted in moist air, as well as in water.

Figure 4 is a schematic of the ADCB wedge test setup. Two kinds of measurements, dry strength, G_{dry}, and wet strength, G_{wet}, were conducted from different ends of the same sample. The dry strength was measured at room temperature and ambient humidity of approx. 20% relative humidity (RH). For dry strength measurements, a razor blade with the thickness of 0.3 mm was inserted at the epoxy/aluminum interface to open the pre-crack and was subsequently forced to propagate by pushing the blade at a speed of 1.9×10^{-6} m/s using an actuator controlled by a motor drive and a computer. The history of the crack growth for at least 3 mm was monitored using a microscope and a video camera, over which 10 crack length measurements were taken with an interval of every 3 min. In the case where the unstable crack propagation (stick-slip and alternating) was observed, this measuring procedure yielded an average G.

A slightly different procedure was followed for the wet strength measurements. The blade was introduced into the starter crack under dry condition, pushed forward at a speed of 7.8×10^{-5} m/s and stopped as soon as the crack started to grow. Several water droplets containing 1% surfactant (Antarox BL-240, Rhodia, Cranbury, NJ, USA) were then drawn from a pipette into the crack, which wetted the crack-tip immediately. The crack grew very quickly at first, and then slowed down to an imperceptible rate within a couple of minutes. The motor drive was then turned back on at 1.9×10^{-6} m/s to force the crack to advance for about 100 μm and the crack length was measured. After the measurement, the velocity of the motor drive was increased stepwise and the above measurements were repeated until the crack advanced to about 10 mm in the sample. This *in situ* measuring procedure allowed us to save the surfaces from the fracture tests under dry condition for further analysis of the locus of failure since the dry strength and wet strength data were obtained from the same sample.

2.6. Characterization

The thickness of the sol–gel films on polished substrate was determined with a Rudolph Research AutoEL® III automatic ellipsometer. Pure aluminum-coated glass slides with the same dimensions as that of 2024-T3 aluminum substrates were employed as the substrates. The thickness of the films on chemically etched substrate was determined by XPS depth profiling. The sputter rate was set at 2.1 nm/min. The Zr signal was monitored until it disappeared and the time was recorded to estimate the thickness.

The substrates before the sol–gel application, the sol–gel-treated substrates before bonding and the fracture surfaces were examined using a Jeol 6300F scanning electron microscope with an Oxford EDS (Energy Dispersive Spectroscopy) system and Scienta ESCA-300 high-resolution X-ray photoelectron spectrometer (XPS). The excitation radiation for the XPS was provided by a monochromatic Al $K\alpha$ X-ray source operated at a constant power of 4.5 kW and a pass energy of 150 eV. The FWHM (full width at half minimum) of the Ag 3d line was approx. 0.53 eV. The spot size was 3 mm$\times$0.5 mm. A flood gun was used to compensate the charging on the polymer samples. All spectra were taken at a 90° take-off angle. A survey scan was taken for each specimen to identify the elements on the surface, followed by detailed high-resolution scan in order to obtain the quantitative information for each element.

3. RESULTS AND DISCUSSION

3.1. Effect of the asymmetry on fracture energy measurement

3.1.1. Fracture energy measurement. For bi-material interfaces, both the fracture energy and the locus of failure depend upon the mode mixity ψ [34]. The

measured fracture energy can increase substantially with a significant mode-II shear component in the fracture process. For systems with large modulus mismatch, cohesive failure is inevitable in almost all the common fracture tests as the crack tends to deflect into the more compliant material (epoxy in the case of epoxy/metal interfaces). This leads to difficulty in interpreting the measured fracture energy data. Nevertheless, Brown [35] demonstrated that the mode-II component could be minimized by properly selecting the thickness ratio of the two materials using an ADCB geometry. This approach was used in the current work.

The data summarized in Fig. 5 show that the asymmetry of the ADCB specimen has a significant effect on measured fracture energy, which goes through a minimum at $h_{\mathrm{Al}}/h_{\mathrm{epoxy}}$ at approx. 0.2 and then increases as the ratio $h_{\mathrm{Al}}/h_{\mathrm{epoxy}}$ increases. The effect is most pronounced when the interface is reinforced with sol–gel film dried at 95°C, 16% RH for 45 min. For a weaker interface reinforced with sol–gel film dried at 23°C, 13% RH for 3 h, the fracture energy does not change significantly for a thickness ratio ranging from 0.1 to 0.4, but it does increase as the thickness ratio is further increased.

The above results can be understood if the effect of mode mixity is considered. Essentially the mode mixity ψ changes with the thickness ratio of the ADCB specimen, with $\psi = 0$ corresponding to pure Mode-I cleavage and yielding the minimum in fracture energy. Xiao *et al.* [30] calculated ψ values as a function of thickness ratios for various model systems with different combinations of materials constants. For the thickness ratio $h_{\mathrm{Al}}/h_{\mathrm{epoxy}}$ range of 0.1 to 0.5 used in the present study, ψ is calculated to vary from $-8°$ to $20°$. The calculated thickness ratio value for $\psi = 0$ of 0.16 agrees reasonably well with our measured value of $h_{\mathrm{Al}}/h_{\mathrm{epoxy}}$ of approx. 0.2.

The ADCB test is not viable for both $h_{\mathrm{Al}}/h_{\mathrm{epoxy}} > 0.5$ and $h_{\mathrm{Al}}/h_{\mathrm{epoxy}} < 0.1$ when using the aluminum thickness of 1.016 mm as in the present study. Too thick an epoxy beam resulted in local plastic deformation of the aluminum beam, while too thin an epoxy beam always broke before the crack propagated. Consequently, only a narrow mode mixity range ($-6°$ to $16°$) was investigated for the relatively weak interface (Fig. 5A), and the measured fracture energies in this range represent a broad minimum. To avoid the above effects, a thicker aluminum substrate should be used.

3.1.2. Locus of failure. The loci of failure are indicative of how the energy is dissipated during the ADCB fracture test. For the specimen with $h_{\mathrm{Al}}/h_{\mathrm{epoxy}} = 0.47$, residual epoxy can be clearly seen on the fractured aluminum surface (Fig. 5B), suggesting that the crack passes through the bulk of the epoxy. By contrast, the locus of failure for the joint with $h_{\mathrm{Al}}/h_{\mathrm{epoxy}} = 0.25$ appears to be interfacial by visual inspection. More detailed information about the failure locus was obtained from the SEM studies. For the joint with $h_{\mathrm{Al}}/h_{\mathrm{epoxy}} = 0.47$, the epoxy is occasionally fractured and very little sol–gel primer is left on the fractured epoxy surface (Fig. 5C). Therefore, some portions of the crack seem to pass close to the

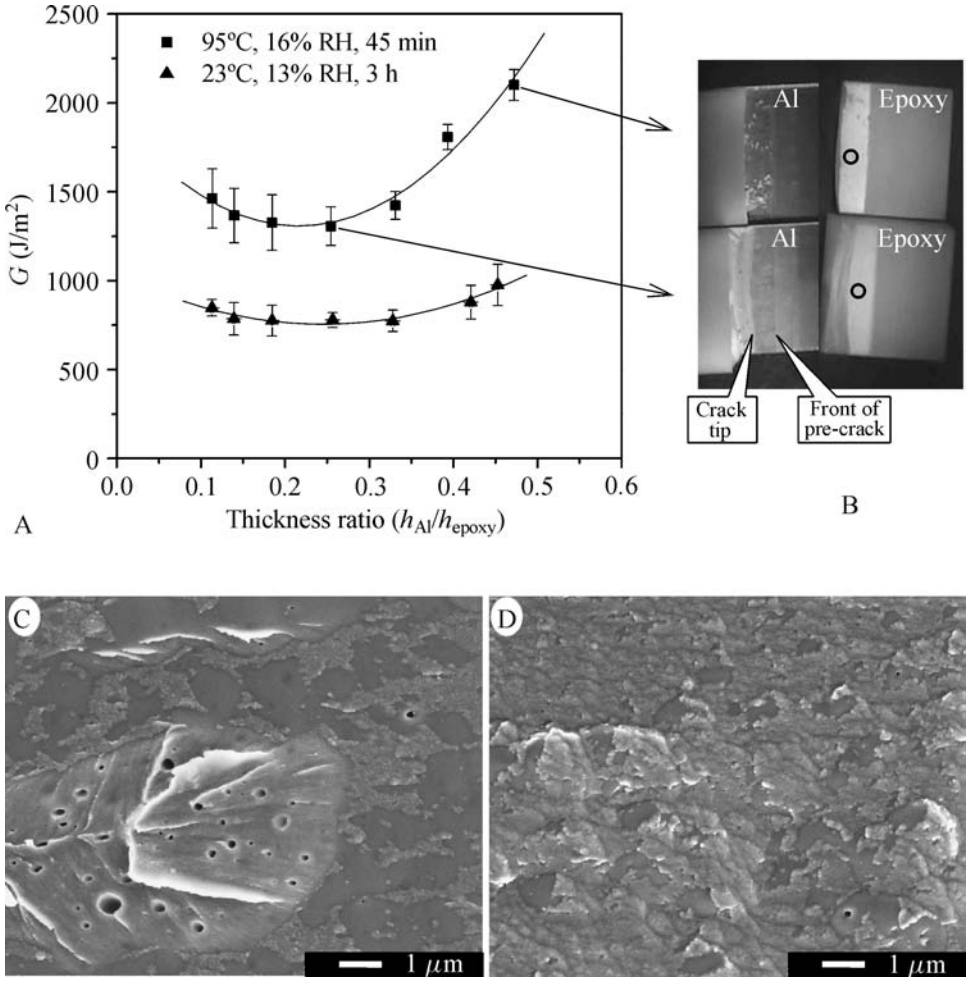

Figure 5. (A) Fracture energy as a function of thickness ratio h_{Al}/h_{epoxy} ($h_{Al} = 1.016$ mm) of the ADCB specimen for two epoxy/aluminum interfaces reinforced by sol–gel films dried at different conditions: (■) 95°C, 16% RH (relative humidity) for 45 min; (▲) 23°C, 13% RH for 3 h. All the films are derived from 2.9% sol–gel solutions on FPL-etched substrates (bare 2024-T3). Each data point was obtained from 4 specimens, with 5 measurements on each specimen. The error bar represents ±1 standard derivation. (B) Fracture surfaces for samples with sol–gel films dried at 95°C: top, $h_{Al}/h_{epoxy} = 0.47$; bottom, $h_{Al}/h_{epoxy} = 0.25$. (C) SEM micrograph taken in the selected area (black circle) in (B) top, $h_{Al}/h_{epoxy} = 0.47$. (D) SEM micrograph taken in the selected area in (B) bottom, $h_{Al}/h_{epoxy} = 0.25$. The flake-like structures are the residual sol–gel layer.

epoxy/sol–gel interface and other portions through the bulk of the epoxy. For the joint with $h_{Al}/h_{epoxy} = 0.25$ the fracture surface on the epoxy side is mostly covered with residual sol–gel film (Fig. 5D). The surface morphology shown in Fig. 5D signifies a cohesive failure in the sol–gel film, as ascertained by the EDS analysis.

Another observation made during visual inspection of the failure locus is the whitening of the fracture surface on the epoxy side (Fig. 5B). Since the sol–gel coating is too thin (approx. 90 nm) to scatter light, this whitening must be due to the local plastic deformation of the epoxy, coupled with cavitation [36], i.e., most of the energy is dissipated by the deformation of the epoxy regardless of whether the fracture occurs at the epoxy/sol–gel interface or in the sol–gel layer. The degree of whitening provides an approximate ranking order for the contribution of the bulk process in the epoxy to the measured value of the fracture toughness of the joint. The greater the whitening, the more the irrecoverable process is occurring in the bulk of the epoxy. The greater degree of whitening for $h_{\mathrm{Al}}/h_{\mathrm{epoxy}} = 0.47$ ($\psi \approx 18°$) than for $h_{\mathrm{Al}}/h_{\mathrm{epoxy}} = 0.25$ ($\psi \approx 4°$) is consistent with the higher toughness observed with the former joint (Fig. 5B). This illustrates why the fracture energy increases significantly, even though the mode mixity increases only slightly for the strong interface.

The above results highlight that the specimen geometry needs to be carefully selected in order to obtain reliable interfacial fracture energies for strong adhesive joints. To minimize the contributions of mode-II components in the measured fracture energies, all of the studies were carried out with the thickness ratio $h_{\mathrm{Al}}/h_{\mathrm{epoxy}}$ approx. 0.16 ($\psi \approx 0°$). The locus of failure for the relatively weak interface reinforced by sol–gel dried at room temperature is a more complicated process due to the unstable crack propagation and will be discussed in detail later in this paper.

3.2. Effect of surface pretreatment and sol–gel concentration

3.2.1. Fracture energy measurement. As described in the Experimental section, four surface pretreatments (polishing, FPL etching, sanding and grit blasting) were investigated. With each surface, both the dry and wet strengths were measured as a function of sol–gel concentration. The results are summarized in Figs 6 and 7, for dry strength and wet strength, respectively. To find out the relationship between the film thickness and sol–gel concentration, nominal film thickness measurements were carried out on two macroscopically flat substrates: the polished substrate with ellipsometry and the FPL-etched substrate with XPS depth profiling. Figure 8 shows that the film thickness increases linearly with the sol–gel concentration for both substrates.

3.2.1.1. Polishing. The fracture toughness of the dry specimens for the polished substrate at first increases linearly with the sol–gel concentration, reaches a maximum value of approx. 600 J/m^2, and then decreases (Fig. 6). This result may be explained by considering the simultaneous effects of interdiffusion of the sol–gel film and the epoxy, as well as cross-linking of the sol–gel [37], both of which are related to the film thickness. The film thickness can affect the kinetics of the condensation cross-linking process, which is controlled by water transport through the sol–gel network. Thinner films cross-link more readily than thicker ones, since the

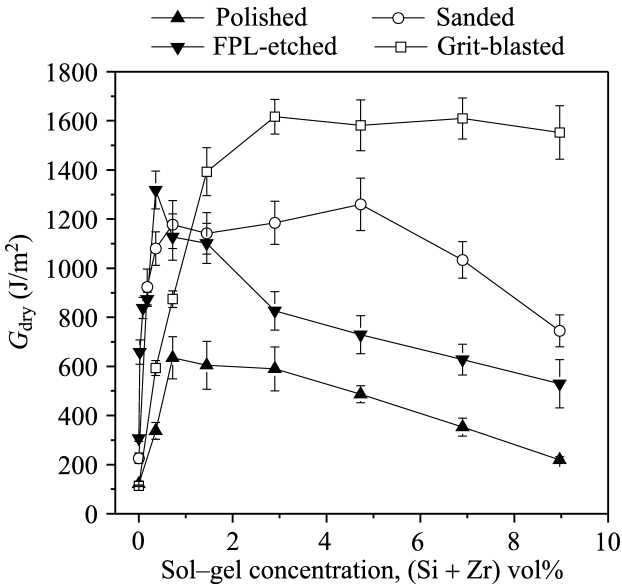

Figure 6. Dry fracture energy as a function of sol–gel precursor concentration and substrate pretreatment for epoxy/aluminum ADCB joints reinforced with sol–gel coatings. The sol–gel concentration is reported as the volume concentration of GPTMS and TPOZ combined. Zero sol–gel concentration means no sol–gel is applied. The substrate is bare 2024-T3 aluminum alloy. Films were dried at room temperature (23°C), 10%–14% RH for 3 h. Each data point was obtained from 10 measurements on every sample. The error bar represents ±1 standard derivation. Substrates are: polished (▲); FPL etched (▼); sanded with 180 grit alumina sandpaper (○); grit-blasted with 50 μm alumina grit (□).

water can escape more easily. This is consistent with the observed decrease of adhesion strength with the increase in the sol–gel concentration. On the other hand, the interdiffusion between the film and the epoxy is compromised as the film thickness decreases, because the film becomes less soluble in epoxy as the cross-link density increases. The trade-off between the cross-linking and interdiffusion, thus, results in a maximum in dry strength in a medium sol–gel concentration range. Additional support for this proposed interplay between cross-linking and interdiffusion will be given later during the analysis of loci of failure.

Another striking feature for the polished substrate, as well as the other pretreatments is that the adhesion strength decreases dramatically in the presence of water (Figs 6 and 7). A maximum plateau region still exists for the wet strength with the fracture energy value of 170 J/m^2, which is 3.5-times lower than that of the dry strength, suggesting that the sol–gel film was not cross-linked well enough for the samples that showed maximum adhesion under dry conditions. Most likely the hydroxyl groups did not condense sufficiently with each other, thus resulting in a film that is soluble in water.

3.2.1.2. FPL etching. The dry (Fig. 6) and wet (Fig. 7) strengths for FPL-etched substrates exhibit trends that differ from those of the polished substrates. They both

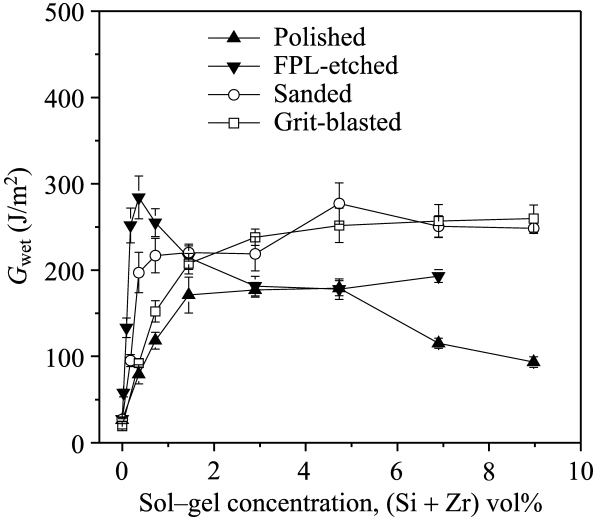

Figure 7. Wet fracture energy as a function of sol–gel precursor concentration and substrate pretreatment for epoxy/aluminum ADCB joints reinforced with sol–gel coatings. The sol–gel concentration is reported as the volume concentration of GPTMS and TPOZ combined. Zero sol–gel concentration means no sol–gel is applied. The substrate is bare 2024-T3 aluminum alloy. Films were dried at room temperature (23°C), 10%–14% RH for 3 h. Each data point was obtained from 5 measurements on every sample. The error bar represents ±1 standard derivation. Substrates are: polished (▲); FPL etched (▼); sanded with 180 grit alumina sandpaper (○); grit-blasted with 50 μm alumina grit (□).

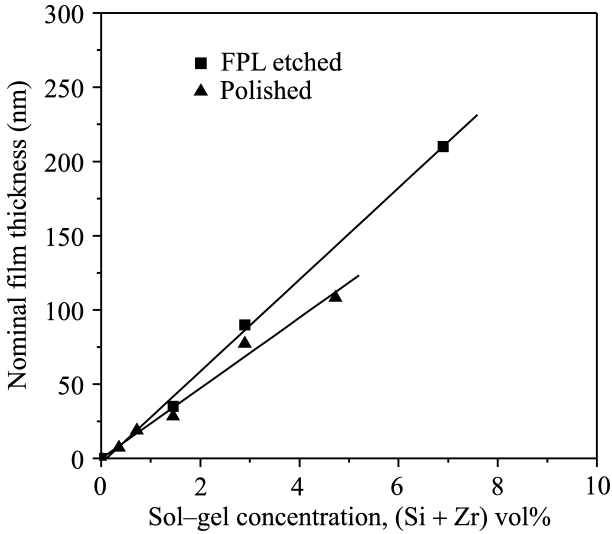

Figure 8. Nominal film thickness as a function of sol–gel concentration for polished (▲) and FPL-etched (■) aluminum substrates (bare 2024-T3), measured by ellipsometry and XPS depth profiling, respectively. A fairly linear relationship between the film thickness and sol–gel concentration is observed for both substrates.

increase significantly within a very narrow concentration range (0–0.2%). The maximum dry strength of 1300 J/m^2 for FPL-etched substrate is more than twice that of the polished substrate, but is found at a sol–gel concentration of 0.36%, which is twice as small as that for the polished substrate. The maximum wet strength of 280 J/m^2 for the FPL-etched substrate is not quite twice that of the polished substrate. The maximum is still at a sol–gel concentration of 0.36% and in this case it is 4-times smaller than for the polished substrate. Another distinct difference between the two types of substrate preparation is that no plateau region is observed for either the dry or wet samples with FPL etched substrates. As the sol–gel concentration increases further, the dry strength decreases rapidly with no significant reinforcement occurring at 9% sol–gel concentration. The wet strength decreases moderately and then levels off at a sol–gel concentration greater than 2.9%.

Differences in the adhesion strengths between the chemically etched and polished substrates motivate a discussion on the effects of surface micro-roughness on adhesion. FPL etching produces a microscopically rough surface that consists of a network of shallow pores and protrusions or whiskers on top of a thin barrier oxide layer [38] (Fig. 13E). As a result, two possible effects are surmised. Firstly, although the drying conditions at the top sol–gel surfaces are the same, the conditions at the local scale of the FPL-etched substrate should be less advantageous for cross-linking than those on a polished mirror-like surface, because the kinetics of the cross-linking process may be retarded due to the transport limitation of the water molecules through the pores and the whiskers. Provided that the cross-link density increases as the film thickness decreases, this effect agrees with the fact that the maximum adhesion strengths are obtained at much lower sol–gel concentrations for the FPL-etched substrate than those for the polished substrate. Secondly, considering that the interdiffusion between the epoxy and sol–gel film could be overshadowed by the interlocking induced by the porous structure on the substrate, the cross-linking of the film is probably more important than the interdiffusion in enhancement of adhesion strength for microscopically rough substrates. This may explain why the adhesion plateau disappears for the FPL-etched substrate. The interlocking on the FPL-etched substrate is evident by the observed cohesive failure in the sol–gel primer for thin films (Fig. 13D).

3.2.1.3. Sanding and grit-blasting. Although the general trend of dry strength observed with the sanded samples is similar to that of the polished samples (Fig. 6), the maximum dry strength (1200 J/m^2) of these samples is twice as large as that of the polished samples. Furthermore, the adhesion plateau is much broader for the sanded samples. This result could be due to a combination of factors arising from the differences in the spreading of the sol–gel, as well as due to the differences in the surface roughness-induced local mode mixity. Grit-blasting produces an extremely tortuous substrate, for which the dry strength increases gradually to a maximum value of 1600 J/m^2 (Fig. 6). This is considerably higher than that of the sanded substrates. Unlike the other three substrates, the adhesion strength for the grit-blasted substrate levels off at a sol–gel concentration of approx. 2.9%.

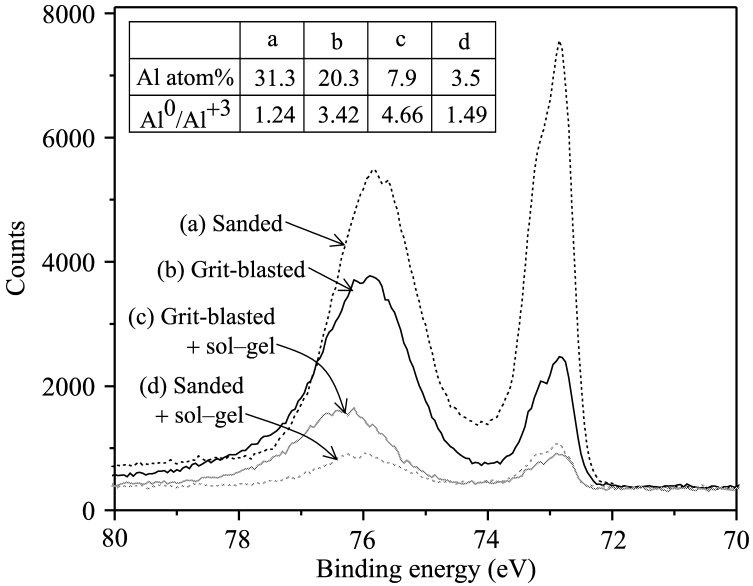

Figure 9. XPS Al_{2p} spectra for various substrates (bare 2024-T3). (a) Sanded only; (b) grit-blasted only; (c) sol–gel-coated grit-blasted substrate; (d) sol–gel-coated sanded substrate. Both films are derived from 2.9% sol–gel solutions. The Al percentage data and the metal/oxide (Al^0/Al^{3+}) ratios for individual surfaces are listed in the inserted table. The Al^0/Al^{3+} is the peak area ratio of the peak at approx. 73 eV to that at about 76 eV, as determined by curve fitting.

The trends of wet strength for both the sanded and grit-blasted substrates are similar to each other (Fig. 7). In both cases, the adhesion strength increases with the sol–gel concentration and then levels off at a value about 240 J/m^2. Nevertheless, for the wet strength as well as for the dry strength (Fig. 6), a sharper transition is observed on the sanded substrates. Figure 9 shows that Al is detected on both sol–gel coated grit-blasted and sanded substrates, with the metal/oxide (Al^0/Al^{3+}) ratios very close to those of the uncoated control sample. This indicates that at the sharp protrusions or high peaks of the rough substrates, the derived films are either so thin that the Al signal can pass through, or the sol–gel does not fully cover the substrate. In both cases, the adhesion strength decreases. Furthermore, at a given sol–gel concentration of 2.9%, the Al amount detected on the coated grit-blasted substrate is about twice as high as that on the coated sanded substrate. Possibly there are more areas where the film is very thin or the sol–gel does not provide as uniform coverage on the grit-blasted substrate as on the sanded substrate; or the film on the grit-blasted substrate is thinner than that on sanded substrate at a given sol–gel concentration. Consequently, a higher concentration of sol–gel solution is needed for a grit-blasted substrate than for a sanded substrate to achieve the maximum adhesion strength.

Another intriguing feature for sanding and grit-blasting is that the wet strengths level off, unlike those observed with polishing and FPL etching (Fig. 7). A simple hypothesis is developed based on these observations by assuming that the dissolu-

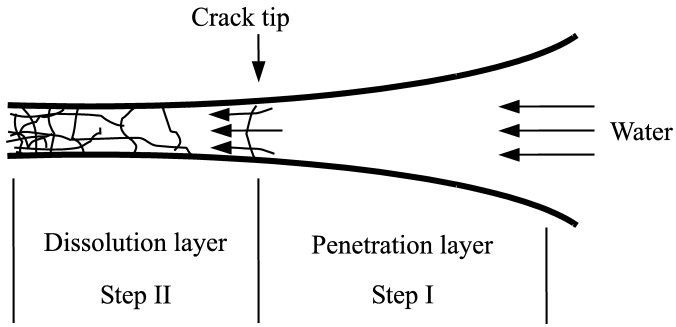

Figure 10. Schematic of the crack-tip region in presence of water.

tion of the sol–gel layer is the dominant mechanism of bond degradation in water. This hypothesis seems to be reasonable as the timescale for the observation is very short (within 5 min). We propose that two rate processes, water penetration from the large crack opening to the crack tip (Step I) and sol–gel dissolution (Step II), compete with each other (Fig. 10). The mechanism underlying Step I depends on the surface asperity of the substrate which can lead to the crack surface contact [39] behind the sharp crack tip, thus affecting the water penetration. The mechanism underlying Step II depends only on the crosslink density and the film thickness. Apparently for relatively thin films, the effect of crosslinking on the rate of sol–gel dissolution is dominant, since water transport can be limited by the partially cross-linked network structure. As the film gets thicker, the effect of thickness comes into play because more water is needed to dissolve the film.

For joints made with polished and FPL-etched substrates, the substrate asperity is very fine, such that the crack surface contact behind the crack-tip can be neglected and the crack-tip seems to be wetted by the water instantaneously. Then, the rate-controlling process is Step II. When the film thickness increases beyond some optimum range, the crosslink density decreases. As a result, the wet strength decreases, since the water transport into the network becomes easier. As the film thickness increases further, the wet strength eventually levels off when some equilibrium between water transport and film dissolution is reached. For joints made by sanded and grit-blasted substrates, the substrate asperity is at a micrometer scale. The crack-surface contact behind the crack-tip can, therefore, inhibit water penetration. Consequently, a competition between Step I and Step II is then inevitable so that the dissolution rate slows down and the effect of cross-linking becomes less important. This might explain why the wet strength for sanded or grit-blasted substrates does not decrease as the sol–gel concentration increases to higher values.

3.2.2. Failure mechanism under dry condition.

3.2.2.1. Polishing. An intriguing observation made during measurements of dry strengths on the polished substrates with sol–gel is that the crack does not propagate in a stable fashion even at a very low driving velocity 1.9×10^{-6} m/s.

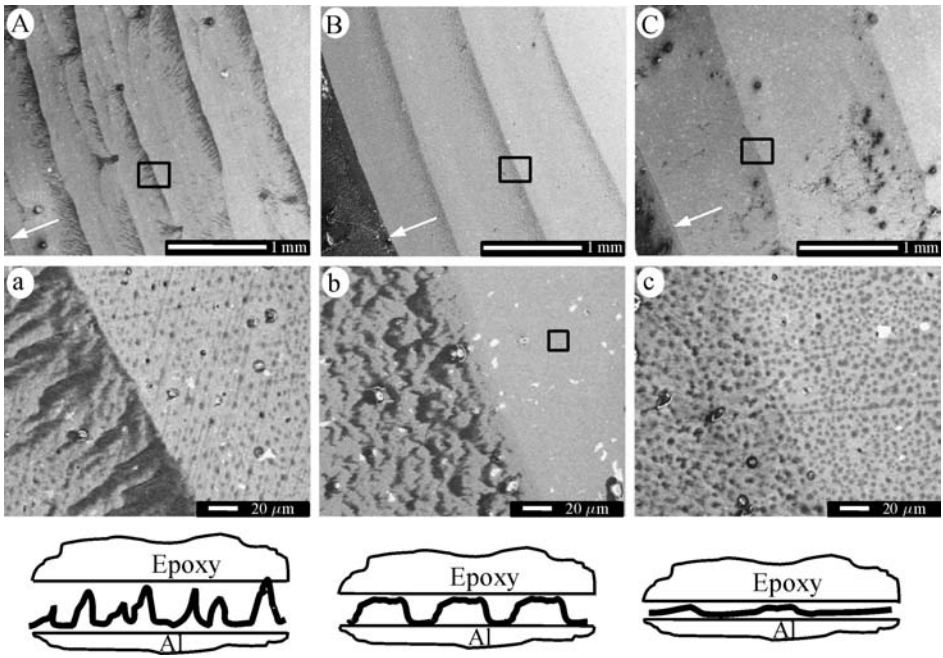

Figure 11. SEM micrographs of fracture surfaces on the aluminum side for joints with films of different thicknesses derived from various concentrations on polished substrates (bare 2024-T3), for which the fracture energies are reported in Fig. 6. (A) 210 nm, 8.97%; (B) 108 nm, 4.73%; (C) 28 nm, 1.45%. (a), (b) and (c) Zoom in the selected areas (as shown by the black frames) in (A), (B) and (C), respectively. The white spots show the intermetallic regions. The arrow indicates the crack-tip and the crack-propagation direction. The schematics are drawn to depict the crack trajectories.

The introduction of a thin sol–gel film between the epoxy and aluminum beams leads to various loci of failure. Figure 11 shows the fractured surfaces on the aluminum side for joints prepared with three different sol–gel solutions, for which the fracture energies are reported in Fig. 6. The dark bands observed visually are ascertained by SEM and XPS analyses to be the fractured residues of the sol–gel layer. A typical stick–slip brittle behavior is observed for the joint with a 210-nm-thick film (Fig. 11A and 11a). The crack remains pinned at the sol–gel/aluminum interface until a sharp and abrupt kink has occurred towards the epoxy/sol–gel interphase region (due to the interdiffusion between the sol–gel film and epoxy, a sharp epoxy/sol–gel interface does not exist). A slip process then takes place, which causes the crack to move close to the sol–gel/aluminum interface at an immeasurably high speed. Repetition of the whole process then leaves behind a serrated broken sol–gel layer on the aluminum surface. A very low fracture energy (220 J/m^2) is observed with this sample.

As the film thickness decreases to 108 nm (Fig. 11B and 11b), an alternating crack trajectory very similar to that observed with the adhesive bonded DCB joints [40–42] was observed. As shown in Fig. 12, no Zr signal was detected by EDS in the selected area about 50 μm ahead of the kink, indicating that the crack

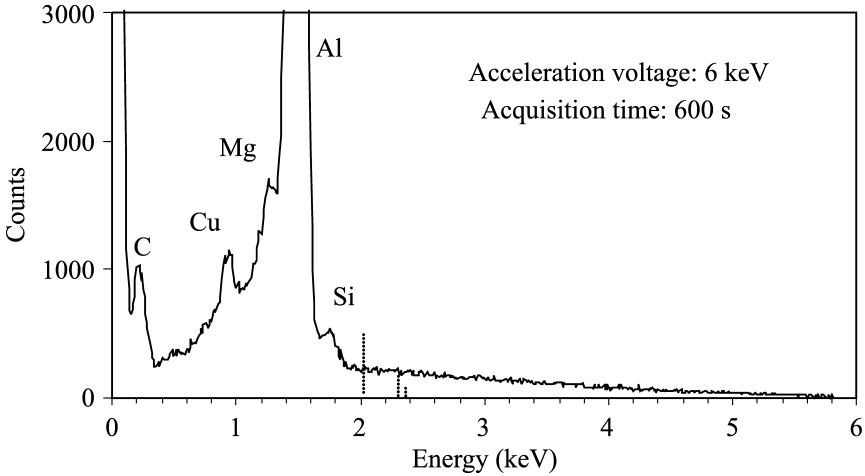

Figure 12. Energy dispersive spectrum taken in the selected area in Fig. 11b (black frame). The dashed lines indicate where the Zr L lines are located. The sample was coated with carbon. A low acceleration voltage of 6 keV was used to keep the surface features visible. No Zr was detected after 600 s collection time. The intermetallic particles contain Cu, Mg and Si elements.

propagates for a certain distance (about 0.3 mm) at the sol–gel/aluminum interface rather than being pinned on it before the kink occurs. The kink flattens out towards the epoxy/sol–gel interphase region, after which it changes direction and starts to propagate parallel to the interface for a distance about 0.3–0.4 mm before deviating away towards the sol–gel/aluminum interface. As a result, the crack appears to be periodically alternating between the sol–gel/aluminum interface and the epoxy/sol–gel interphase region.

As the film thickness decreases to 28 nm (Fig. 11C and 11c), the stick-slip behavior appears again. However, the kink is smoother, and the slip velocity is apparently much lower than that observed for the joint with thicker films. Consequently, the kinking pattern becomes rather regular with a characteristic wavelength about 1.5 mm. The failure here is mostly cohesive within the sol–gel bulk and occasionally epoxy residues can be seen on fractured aluminum surface (Fig. 11C). Maximum fracture energy is obtained for this sample.

3.2.2.2. FPL etching. The locus of failure for sol–gel reinforced joints prepared using FPL-etched substrates shows an interesting transition from a brittle to a ductile failure as the film thickness decreases. In the optical photograph of Fig. 13A, an alternating crack is observed for the joint with a 270 nm thick sol–gel film on FPL etched substrate. The white bands on the fractured epoxy side (Fig. 13B) are about 150 μm long and represent areas with thick residual sol–gel layers, thus suggesting an interfacial failure at the sol–gel/aluminum interface. This conjecture is further reinforced by the SEM micrograph of highly porous texture of the top surface (Fig. 13C), which is almost a replica of the FPL-etched control surface (Fig. 13E). Right after the white band a kink can be seen towards the epoxy bulk

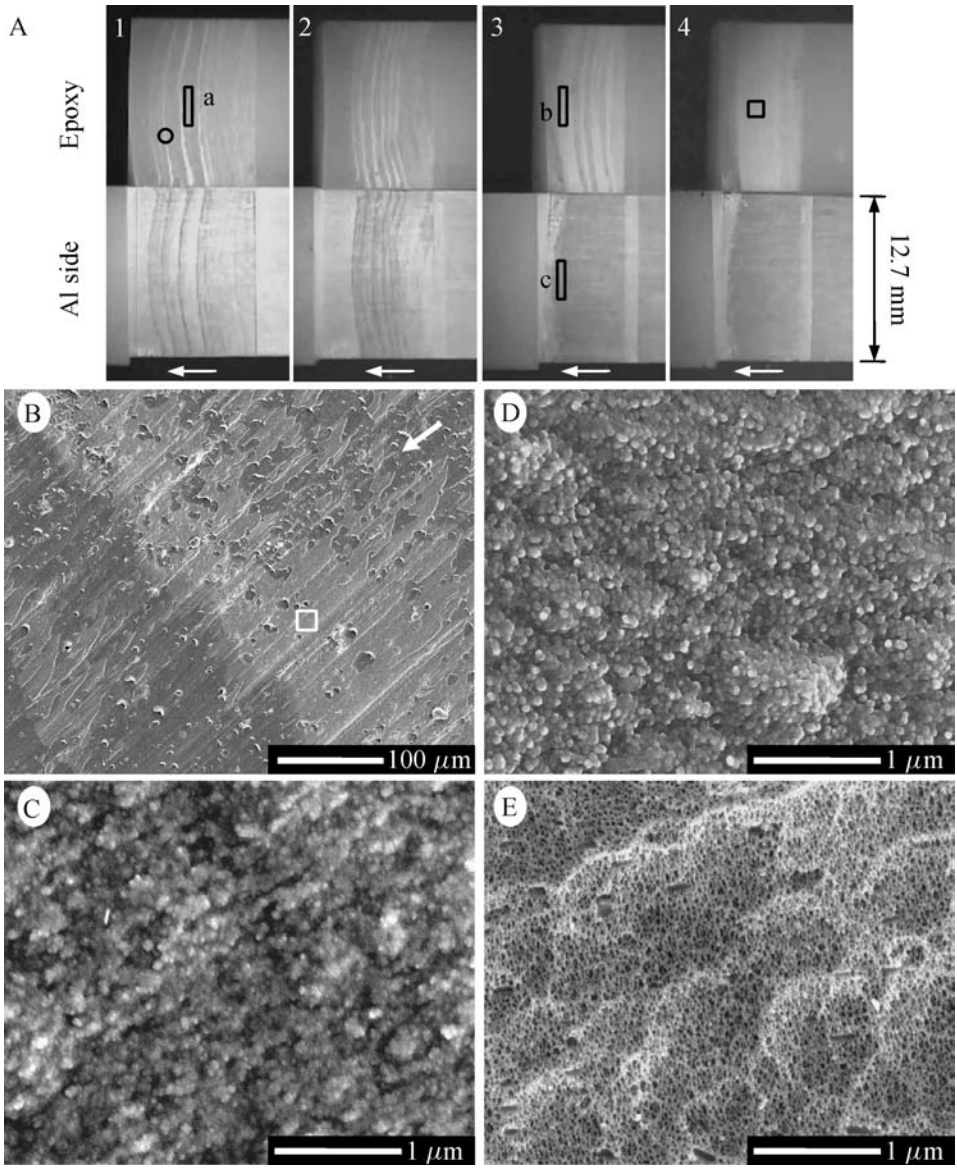

Figure 13. Fracture surfaces of the sol–gel reinforced epoxy/aluminum ADCB joints prepared with FPL-etched substrates (bare 2024-T3) compared to FPL-etched substrate before sol–gel application. Fracture energies are reported in Fig. 6. The arrow indicates the direction of crack propagation. (A) Optical photographs of fracture surfaces for joints with films of different thicknesses derived from various sol–gel concentrations: (1) 270 nm, 8.97%; (2) 150 nm, 4.73%; (3) 30 nm, 1.45%; (4) 7 nm, 0.36%. The films are dried at 23°C, 13% RH for 3 h. (B) SEM photograph taken at the selected area (black circle) on (A1). (C) SEM photograph taken at the selected area (white frame) on (B). (D) SEM photograph taken at the selected area on (A4). (E) SEM photograph for the FPL-etched substrate prior to sol–gel application.

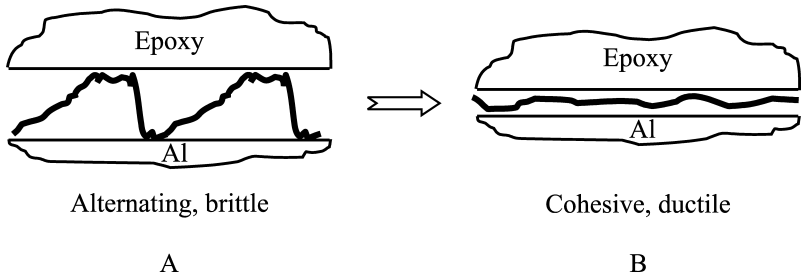

Figure 14. Schematic of failure mechanisms *vs.* sol–gel film thickness for sol–gel reinforced epoxy/aluminum ADCB joints prepared using FPL-etched substrates (bare 2024-T3).

indicating that the crack propagated in the epoxy/sol–gel interphase region. As both the Si and Zr signals are detected on the selected area between the white bands (Table 4), the crack apparently moves back to the sol–gel/aluminum interface and the sol–gel film is cracked diagonally in the middle. It should be noted that the fracture process for the FPL etched substrate is not stable. However, crack propagation differs markedly from the stick–slip behavior of the polished substrate. Here, the crack tends to advance at the sol–gel/aluminum interface for a short distance (approx. 150 μm), while an unstable process occurs in the epoxy/sol–gel interphase region where the crack propagates a relatively long distance (0.5–0.6 mm) at a speed markedly higher than the driving velocity. Based upon these facts, the schematic of the crack trajectory is shown in Fig. 14A.

In the other extreme, SEM investigation of the failure locus for the joint with the very thin film (7 nm) shows that it is cohesive within the sol–gel film (Fig. 13A4). The surface morphology and topography for the whitened fractured surface on the epoxy side (Fig. 13D) differ significantly from those for 270 nm film (Fig. 13C). No bulk epoxy can be seen. Furthermore, the micro-structures on this surface are noticeably larger than those on the FPL control surface prior to sol–gel treatment (Fig. 13E), which suggests that the sol–gel trapped in these tiny pores is never pulled out. Indeed, inspection of the aluminum side (not shown) demonstrates that the whisker structure that can be easily observed on the FPL control surface is completely buried by the sol–gel coating and, thus, is invisible under SEM. For the sol–gel coatings there apparently is a critical length scale of the microstructure on the substrate, below which further adhesion enhancement does not occur. The crack trajectory for the thin film is shown schematically in Fig. 14B.

As the film thickness decreases from 270 nm to 7 nm, the width of the white bands on the epoxy side clearly increases and eventually spreads over the whole fracture surface (Fig. 13A1–A4). This intriguing observation implies that a transition of locus of failure, from alternating failure between the interfaces to cohesive failure in the sol–gel film, occurs as the film thickness decreases. The white bands on the epoxy side for the joint reinforced with 30-nm-thick film (Fig. 13A3) become wide enough for XPS analysis, thus enabling clearer identification of the locus of failure.

Table 4.
XPS elemental analysis results (in at%) for the control surfaces and fracture surfaces of the sol–gel-reinforced epoxy/aluminum (bare 2024-T3) ADCB joints prepared with FPL-etched substrates

Surface analyzed	C	N	O	Si	Zr	Al	Cu
Epoxy bulk	85.7	5.2	9.1				
a[1]	68.3	7.8	18.8	4.3	0.8		
b[2]	66.8	5.1	21.8	2.9	0.7	2.5	0.2
c[3]	57.1	4.3	24.9	3.5	0.7	9.4	0.2
Film before bonding[4]	51.0		35.4	9.3	2.4	1.7	0.2
FPL etched only	22.7		47.9	0.5		28.6	0.3

[1,2,3]Selected areas as shown in Fig. 13A1 and A3 (black frames).
[4]Sol–gel film on FPL-etched substrate before bonding; derived from 1.45% solution.

Analyzing the atomic constituents obtained from the selected area of the epoxy side and its counterpart on the aluminum side (Table 4), Si and Zr were detected on both sides with amounts comparable to each other. The amount of Al detected on the aluminum side (9.4%) is much lower than that detected on the FPL control surface (28.6%), but much higher than that detected on the 'film before bonding' control surface (1.7%). These two observations suggest that the sol–gel film is cracked in the middle. Small amounts of Al (2.5%) and Cu (0.2%), which can only come from the aluminum substrate, were found on the epoxy side, revealing that the fracture occurred also to a small extent in the aluminum oxide layer.

The amount of N detected on the aluminum side (4.3%), which is attributed to the curing agent and/or the toughener CTBN, is as high as that detected on the epoxy bulk control. The amount of C on the aluminum side (57.1%) is higher than that on the sol–gel control. These results suggest that the crack passes through the bulk of the epoxy. SEM inspection, however, does not support this conjecture, since no epoxy can be seen on the aluminum side. Additionally, the morphology and the micro-topography of the white bands on the epoxy side for this sample (not shown) are almost identical to those obtained from the joint made with a 7 nm film (shown in Fig. 13D), for which the fractured sol–gel layer is continuous and no epoxy bulk is exposed. A plausible explanation is that the uncured resin monomer, as well as the curing agent are able to diffuse into the sol–gel film during the curing process, thus leading to interdiffusion between the sol–gel film and epoxy.

Several studies have concluded that the stability of a crack is directly controlled by the non-singular stress acting parallel to the crack line [44–48]. An analytic solution for the crack behavior in this study is complicated since the mechanical properties, including the residual stresses, of the thin films employed here cannot be easily determined. However, the general effects of the film thickness on fracture energy can be explained qualitatively.

The extremely brittle fracture behavior and low fracture energies observed with the thick sol–gel films strongly suggest that the films are not fully crosslinked. An analogy to the curing of a thermosetting resin system could be made for sol–gel drying behavior. According to the Time–Temperature–Transformation principle

[49], the resin can simply vitrify and remain glassy for very long time if the curing temperature is lower than the '$T_{g\infty}$'. The partially cross-linked resin in this state can be extremely brittle. Sol–gel drying may proceed in a similar fashion. While some studies have indicated that the room temperature dried sol–gel film could be co-cured with the applied epoxy resin (data not shown), the results shown in Fig. 5A do not support this speculation, since the fracture energy for the film dried at elevated temperature (95°C) is much higher than that dried at room temperature. Nevertheless, the maximum fracture energy (1300 J/m^2) observed on FPL substrates in Fig. 6 for the film dried at room temperature is as high as that for the film dried at 95°C (Fig. 5A), but at a much lower sol–gel concentration. Taken together with the observed cohesive ductile failure in thin films, these results further support the conjecture that the crosslink density increases as the film thickness decreases.

3.2.2.3. Sanding and grit-blasting. In the ADCB dry test, the joints prepared with sanded and grit-blasted substrates showed much simpler fracture behavior than those with polished and FPL-etched substrates. The alternating crack trajectory was observed only for the joint prepared with sanded substrate at a high sol–gel concentration (8.97%). The crack propagated in a very stable fashion for all the joints prepared with grit-blasted substrates. Evidently, the surface roughness plays an important role in crack stability.

Figure 15 depicts the surface topography for the fracture surface on the aluminum side of a joint prepared at a sol–gel concentration of 2.9% compared to the sanded substrate prior to sol–gel treatment. Apparently, there is no significant difference in topography between these two surfaces under SEM. However, residual epoxy can be seen sporadically with the sharply edged protrusions, indicating partial fracture of the epoxy side.

The XPS results on the fracture surfaces on both aluminum and epoxy sides of the same sample along with the controls (sanded surfaces prior to sol–gel and with

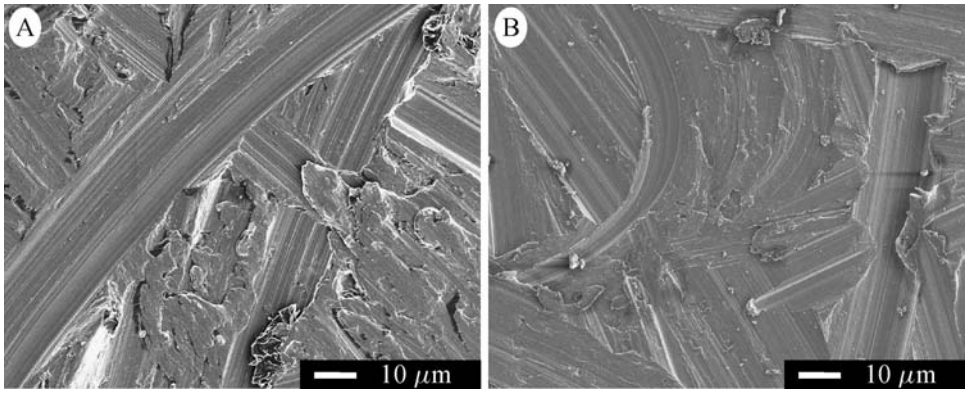

Figure 15. SEM micrograph of the fracture surface on the aluminum side for joint reinforced by sol–gel film derived from 2.9% sol–gel concentration on the sanded substrate (A) compared to that of the sanded substrate prior to sol–gel treatment (B).

sol–gel, epoxy bulk) are shown in Table 5. Si and Zr were detected on both the aluminum and epoxy sides. The amount of Al (13.1%) detected on the aluminum side is much lower than that detected on the sanded-only surface (32.6%), but much higher than that detected on the 'film before bonding' control surface (3.5%). Additionally, a considerable amount of Mg, the minor alloy element from the aluminum substrate, is found on the sanded-only surface but not on the aluminum side. All these results suggest that a cohesive failure in the sol–gel film is the main failure mechanism with these samples. The existence of N and the high C amount (50.7%) on the aluminum side as compared to the sanded-only surface may not be solely attributable to the occasionally observed epoxy under SEM. Diffusion of the monomer resin and the migration of the curing agent during the cure can also contribute. Detection of an anomalously high N amount on the epoxy side as compared to the epoxy bulk control also supports this conjecture. The amounts of Zr and Si detected on the epoxy side are higher than those detected on the aluminum side, indicating the possibility that the fracture occurred closer to the aluminum substrate than to the epoxy. The lack of the Al, Mg and Cu signals on the epoxy side suggests that no cohesive failure occurred on the aluminum side. Based upon these results, a schematic is shown in Fig. 16A to illustrate the crack trajectory.

Figure 17 shows two SEM micrographs. The first is taken from the fractured surfaces on the aluminum side of a joint prepared with grit-blasted substrate at sol–gel concentration of 2.9%. The second is the grit-blasted substrate before sol–gel treatment. The 'hills' and 'valleys' created by the grit blasting made the surface extremely tortuous (Fig. 17B). This topography is retained on the fractured surface (Fig. 17A). However, residual epoxy that was not pulled off can be clearly seen in

Table 5.
XPS elemental analysis results (in at%) for the control surfaces and fracture surfaces for sol–gel-reinforced epoxy/aluminum (bare 2024-T3) ADCB joints prepared with sanded substrate, 2.9% sol–gel concentration

Surface analyzed	C	N	O	Al	Si	Zr	Mg	Cu
Sanded only	23.2	0.9	41.4	32.6	0.1		1.6	0.2
Film before bonding	52.6		33.3	3.5	8.6	2.0		
Fractured (aluminum)	50.7	6.0	25.9	13.1	3.6	0.8		0.1
Fractured (epoxy)	66.0	7.9	21.0		4.0	1.2		
Epoxy bulk	85.7	5.2	9.1					

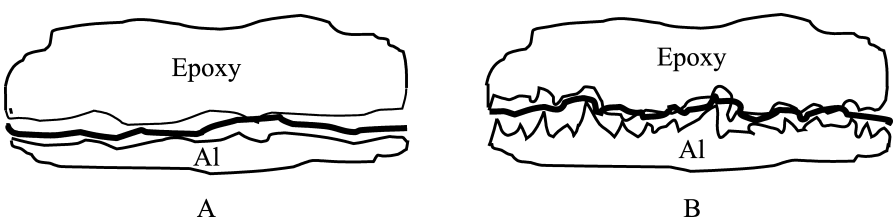

Figure 16. Schematics of the failure mechanisms of sol–gel reinforced epoxy/aluminum ADCB joints prepared with sanded and grit-blasted substrates (bare 2024-T3). (A) sanded, (B) grit-blasted.

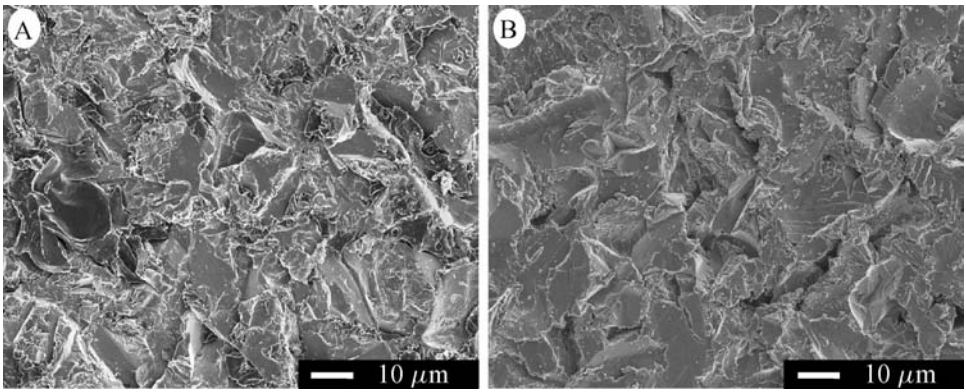

Figure 17. SEM micrograph of the fractured surface on the aluminum side for a joint reinforced by sol–gel film derived from 2.9% sol–gel concentration on grit-blasted substrate (A) compared to that of the grit-blasted substrate prior to sol–gel treatment (B).

Table 6.
XPS elemental analysis results (in at%) for the control surfaces and fractured surfaces for grit-blasted epoxy/sol–gel/aluminum (bare 2024-T3) joints, 2.9% sol–gel concentration

Surface analyzed	C	N	O	Al	Si	Zr	Mg	Cu	Na	S
Grit-blasted only	31.3		40.7	20.3	1.6		1.2	0.1	3.1	1.6
Film before bonding	50.1		33.7	7.9	6.4	1.8		0.1		
Fractured (aluminum)	56.1	4.2	26.5	10.3	2.0	0.5				
Fractured (epoxy)	72.8	4.4	18.4	2.4	1.7	0.5	0.4			
Epoxy bulk	85.7	5.2	9.1							

the ‘valleys’, at an amount noticeably higher than that on the sanded substrate of Fig. 15. This fact is consistent with the very high fracture energy measured on the grit-blasted sample. It is likely that the high asperity of the surface changed the local mode mixity and effectively enhanced the fracture energy.

The XPS results on the fracture surfaces and controls (grit-blasted surfaces prior to sol–gel and with sol–gel, as well as epoxy bulk) are shown in Table 6. Following the same elemental analysis as was carried out for the sanded substrate, the locus of failure is partially within the sol–gel film and partially within the epoxy bulk. The schematic of the crack trajectory is shown in Fig. 16B.

Three other points of interest from Table 6 should be noted here. Firstly, the high C amount detected from the grit-blasted surface (without sol–gel treatment) indicates high levels of hydrocarbon contamination. Na and S found on the grit-blasted control surface could be from the blasting medium, as reported by Possart *et al.* [50]. Secondly, on both the aluminum- and epoxy-fractured surfaces, no Na or S are detected. One possibility is that these elements tend to accumulate in the ‘valleys’, are buried by the residual epoxy and, therefore, cannot be detected by XPS. They could also be displaced by the sol–gel solution upon application. Finally, Mg and Al are detected on the epoxy side, which suggests that the crack

Table 7.
XPS elemental analysis results (in at%) for the sol–gel control surfaces and fracture surfaces for epoxy/sol–gel/aluminum (bare 2024-T3) joints with various pretreatments failed in presence of water, 2.9% sol–gel concentration

Surface analyzed		C	N	O	Al	Si	Zr	Mg	Cu	Na
Polished	Film before bonding	55.9		32.4		9.3	2.4			
	Fractured (aluminum)	61.5	4.7	22.9	2.9	6.4	1.6			
	Fractured (epoxy)	75.3	4.6	16.7		2.5	0.9			
FPL-etched	Film before bonding	53.4		33.6	0.9	9.3	2.4		0.4	
	Fractured (aluminum)	62.0	7.2	22.8	3.6	3.2	0.9		0.3	
	Fractured (epoxy)	67.4	7.0	20.1	1.1	3.4	1.0			
Sanded	Film before bonding	52.6		33.3	3.5	8.6	2.0			
	Fractured (aluminum)	60.4	3.8	24.1	6.3	4.8	0.6			
	Fractured (epoxy)	68.5	5.5	21.1	0.9	3.1	0.9			
Grit-blasted	Film before bonding	50.1		33.7	7.9	6.4	1.8		0.1	
	Fractured (aluminum)	49.2	3.9	30.7	12.0	2.5	0.5	0.6		0.6
	Fractured (epoxy)	69.4	4.8	21.0	2.2	2.0	0.5			0.2
Epoxy bulk control		85.7	5.2	9.1						

passes partly through the oxide layer of the aluminum substrate. The Al signal, however, could also be from the loosely-bonded alumina grit trapped during the blasting process as well.

3.2.3. Failure mechanism in wet condition. To understand the mechanisms of failure for the sol–gel reinforced joints under wet condition, visual inspection and XPS analysis were carried out on fracture surfaces obtained from various samples. The XPS results with samples prepared from 2.9% sol–gel solution are shown in Table 7. The results on the pretreated surfaces with films derived from the same solution and the epoxy bulk are also listed as controls.

According to the visual inspection, all the joints fail along the epoxy/aluminum interface. The whitening on the epoxy side disappears. For sanded and grit-blasted samples, no epoxy can be seen on the aluminum side under SEM. Si and Zr are detected on the fractured surfaces of both aluminum and epoxy at comparable amounts for all the pretreatments. All these observations suggest that the sol–gel films fracture in the middle, which is consistent with the mechanism of sol–gel dissolution. The Al signal is detected on the epoxy side for FPL etched, sanded, and grit-blasted substrates, indicating that the aluminum oxide layer could be hydrolyzed and become the weak link in the water.

A considerable amount of N is found on the aluminum side of the fracture surfaces for all the pretreatments even when failure occurs in the wet condition. Since the toughened epoxy is unlikely to crack at such a low crack driving energy of 250 J/m^2, the only plausible source of N is the curing agent from the epoxy system, which seems to migrate into the sol–gel film. The high carbon amount detected on the aluminum side further supports the argument that the monomer resin diffused into the sol–gel layer during the curing process.

4. CONCLUSIONS

ADCB wedge tests illustrate that both the fracture energy and the locus of failure are highly dependent upon the mode mixity for an epoxy/aluminum interface with strong adhesion, resulting from the application of the zirconium/silicon based sol–gel coatings. ADCB specimens offer the unique advantage in forcing the crack to propagate close to the epoxy/aluminum interface, so that the effects of surface pretreatments and the processing conditions of the adhesion promoter can be evaluated.

The dry and the wet strengths of the epoxy/aluminum joints depend on both the sol–gel concentration, as well as the surface pretreatment. The film thickness increases linearly with the sol–gel concentration. Thinner films are more fully cross-linked, thus giving higher adhesion strength than those obtained with thicker films. The differences in the wet strengths for the sol–gel reinforced joints for various surface pretreatments strongly suggest that the sol–gel film can be dissolved to some extent in water. This is also supported by the XPS results.

Another important feature of this study is the alternating crack trajectory between the epoxy/sol–gel and sol–gel/aluminum interfaces, a behavior which was especially prevalent in the polished and FPL-etched substrates. Although the origin of the alternating crack trajectory observed in the present system is not fully analyzed at this point, the brittle *versus* ductile crack behavior associated with the failure process reveals important information about how the structure of the sol–gel film affects the adhesion strength.

Acknowledgements

Financial support for this work provided by The Boeing Company and the Polymer Interface Center at Lehigh University is gratefully acknowledged. We would also like to thank Prof. R. A. Pearson of Lehigh University for helpful discussions, Dr. A. C. Miller of Lehigh University for his assistance in XPS studies and Jacob Grob of The Boeing Company for helpful discussions and training on processes.

REFERENCES

1. A. Baldan, *J. Mater. Sci.* **39**, 1 (2004).
2. E. P. Plueddemann, *Silane Coupling Agents*, 2nd edn. Plenum Press, New York, NY (1991).
3. M. J. Owen, in: *Adhesion Science and Engineering 2*, *Surface, Chemistry & Applications*, M. K. Chaudhury and A. V. Pocius (Eds), p. 403. Elsevier Science, Amsterdam (2002).
4. M.-L. Abel, J. F. Watts and R. P. Digby, *J. Adhesion* **80**, 291 (2004).
5. A. Namkanisorn, A. Ghatak, M. K. Chaudhury and D. H. Berry, *J. Adhesion Sci. Technol.* **15**, 1725 (2001).
6. K. Y. Blohowiak, J. H. Osborne, K. A. Krienke and D. F. Sekits, in: *Proc. 28th Int. SAMPE Symp.*, p. 440 (1996).
7. K. Y. Blohowiak, K. A. Krienke, J. H. Osborne, J. J. Mazza, G. B. Gaskin, J. R. Arnold, W. S. DePiero and J. Brescia, in: *Proc. The Second Joint NASA/FAA/DoD Conference on Aging Aircraft*, p. 313 (1998).

8. J. H. Osborne, K. Y. Blohowiak, S. R. Taylor, C. Hunter, G. Bierwagen, B. Carlson, D. Bernard and M. S. Donley, *Prog. Organic Coatings* **41**, 217 (2001).
9. K. Y. Blohowiak, J. H. Osborne and K. A. Krienke, US Patent No. 5,814,137 (1998).
10. K. Y. Blohowiak, J. H. Osborne and K. A. Krienke, US Patent No. 5,849,110 (1998).
11. K. Y. Blohowiak, J. H. Osborne and K. A. Krienke, US Patent No. 5,939,197 (1999).
12. K. Y. Blohowiak, J. H. Osborne and K. A. Krienke, US Patent No. 6,037,060 (2000).
13. R. B. Greegor, K. Y. Blohowiak, J. H. Osborne, K. A. Krienke and J. T. Cherian, *J. Sol-Gel Sci. Technol.* **20**, 35 (2001).
14. C. J. Brinker and G. W. Scherer, *Sol-Gel Science: The Physics and Chemistry of Sol-Gel Processing*. Academic Press, San Diego, CA (1990).
15. T. L. Metroke, R. L. Parkhill and E. T. Knobbe, *Prog. Organic Coatings* **41**, 233 (2001).
16. K. Y. Blohowiak, L. Cadwell-Stancin, R. A. Anderson, C. M. Mazzitelli, K. Preedy, J. W. Grob and M. Glidden, in: *Proc. 47th Int. SAMPE Symp.*, p. 279 (2002).
17. D. B. McCray and J. J. Mazza, in: *Proc. 45th Int. SAMPE Symp.*, p. 42 (2000).
18. K. E. Huber, D. B. McCray and R. Srinivasan, in: *Proceedings of Processing and Fabrication of Advanced Materials IX*, p. 53 (2001).
19. H. R. Brown, *Macromolecules* **22**, 2859 (1989).
20. C. Creton, E. J. Kramer, C.-Y. Hui and H. R. Brown, *Macromolecules* **25**, 3075 (1992).
21. F. Xiao, C.-Y. Hui, J. Washiyama and E. J. Kramer, *Macromolecules* **27**, 4382 (1994).
22. B. Bernard, H. R. Brown, C. J. Hawker, A. J. Kellock and T. P. Russell, *Macromolecules* **32**, 6254 (1999).
23. C. Creton, E. J. Kramer, H. R. Brown and C.-Y. Hui, *Adv. Polym. Sci.* **156**, 53 (2001).
24. R. Bagheri and R. A. Pearson, *Polymer* **37**, 4529 (1996).
25. R. Bagheri and R. A. Pearson, *Polymer* **41**, 269 (2000).
26. K. Y. Blohowiak, J. H. Osborne and K. A. Krienke, US Patent No. 5,869,141 (1999).
27. R. G. Dillingham and F. J. Boerio, in: *Silanes and Other Coupling Agents*, K. L. Mittal (Ed.), p. 493. VSP, Utrecht (1992).
28. J. D. Venables, *J. Mater. Sci.* **19**, 2433 (1984).
29. M. F. Kanninen, *Int. J. Fracture* **9**, 83 (1973).
30. F. Xiao, C.-Y. Hui and E. J. Kramer, *J. Mater. Sci.* **28**, 5620 (1993).
31. S. Zhang, R. Panat and K. J. Hsia, *J. Adhesion Sci. Technol.* **17**, 1685 (2003).
32. ASM, *Metals Handbook*, 10th edn., Vol. 2, p. 70. ASM International, Materials Park, OH (1990).
33. *Encyclopedia of Polymer Science and Engineering*, 2nd edn, Vol. 16, p. 737. Wiley, New York, NY (1985).
34. J. W. Hutchinson and Z. Suo, *Adv. Appl. Mech.* **29**, 63 (1991).
35. H. R. Brown, *J. Mater. Sci.* **25**, 2791 (1990).
36. A. J. Kinloch and R. J. Young, *Fracture Behaviour of Polymers*. Elsevier, New York, NY (1983).
37. M. K. Chaudhury, T. M. Gentle and E. P. Plueddemann, *J. Adhesion Sci. Technol.* **1**, 29 (1987).
38. G. D. Davis and J. D. Venables, in: *Adhesion Science and Engineering 2, Surface, Chemistry & Applications*, M. K. Chaudhury and A. V. Pocius (Eds), p. 947. Elsevier, Amsterdam (2002).
39. A. G. Evans and J. W. Hutchinson, *Acta Metall.* **37**, 909 (1989).
40. H. Chai, *Int. J. Fract.* **32**, 211 (1987).
41. H. C. Cao and A. G. Evans, *Mech. Mater.* **7**, 295 (1989).
42. J. S. Wang and Z. Suo, *Acta Metall. Mater.* **38**, 1279 (1990).
43. B. Chen and D. A. Dillard, *Int. J. Adhesion Adhesives* **21**, 357 (2001).
44. B. Cotterell and J. R. Rice, *Int. J. Fract.* **16**, 155 (1980).
45. N. A. Fleck, J. W. Hutchinson and Z. Suo, *Int. J. Solids Struct.* **27**, 1683 (1991).
46. A. R. Akisanya and N. A. Fleck, *Int. J. Fract.* **55**, 29 (1992).
47. A. R. Akisanya and N. A. Fleck, *Int. J. Fract.* **58**, 93 (1992).
48. B. Chen and D. A. Dillard, in: *Adhesion Science and Engineering 1, The Mechanics of Adhesion*, D. A. Dillard and A. V. Pocius (Eds), p. 389. Elsevier, Amsterdam (2002).

49. J. K. Gillham, In: *Developments in Polymer Characterization*, Vol. 3, J. V. Dawkins (Ed.), p. 159. Applied Science, Harlow (1982).
50. W. Possart, C. Bockenheimer and B. Valeske, *Surface Interface Anal.* **33**, 687 (2002).
51. Y. Sha, C.-Y. Hui, E. J. Kramer, S. F. Hahn and C. A. Berglund, *Macromolecules* **29**, 4728 (1996).
52. S. Timoshenko, *J. Opt. Soc. Am.* **11**, 233 (1925).

APPENDIX: EVALUATION OF G_T

One major concern about the ADCB wedge test is that the specimen becomes slightly warped when cooled from the cure temperature to room temperature because of the thermal expansion mismatch between the aluminum and epoxy. The energy release rate given by equation (1) assumes that the ADCB specimen is in a stress-free state and only the flat specimen is considered. This may not be a good approximation for the epoxy/aluminum system. Therefore, one needs to estimate the energy release rate due to the thermal loading. Sha *et al.* [51] showed that this could be done using the fracture mechanics concept. However, some of the parameters in their equation have to be calculated numerically, which makes it inconvenient. Following Timoshenko's early work [52] on calculating the radius of curvature of a bimaterial strip under thermal loading, we propose a much simpler analysis of the problem.

Figure A1 illustrates the fundamental mechanics problem of the ADCB specimen under both wedge and thermal loadings. The total energy is stored in both the bonded and debonded portions of the beam. It is evident that only the bonded portion has the thermal loading, which is equivalent to the application of loads (P, M_1, and M_2) as shown in Fig. A1. Thus, the energy release rate due to the thermal loading, G_T, can be calculated by

$$G_T = -\frac{1}{B}\left(\frac{\partial U_b}{\partial a}\right), \tag{A1}$$

where B is the width of the specimen, U_b is the energy stored in the bonded portion and a is the crack length.

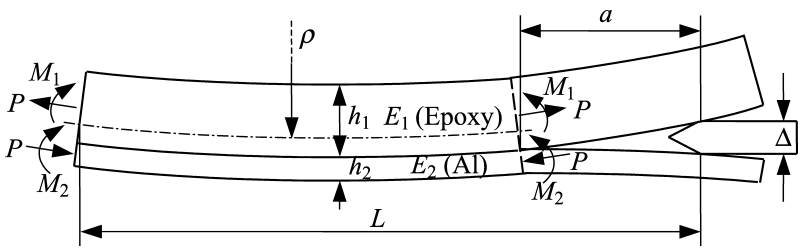

Figure A1. The geometry of the warped ADCB specimen.

M_1, M_2 and P are given by the following equations:

$$M_1 = \frac{E_1 I_1}{\rho};\ M_2 = \frac{E_2 I_2}{\rho};$$

$$P = \frac{2}{\rho}\left(\frac{E_1 I_1 + E_2 I_2}{h_1 + h_2}\right), \tag{A2}$$

where $I = (1/12)Bh^3$, ρ is the radius of curvature of the warped beam, E is Young's modulus, h is the beam thickness, and subscripts 1, 2 denote epoxy and aluminum, respectively.

The energy stored in the bonded portion U_b is given by

$$\begin{aligned} U_b &= \frac{P^2(L-a)}{2Bh_1E_1} + \frac{P^2(L-a)}{2Bh_2E_2} + \frac{M_1^2(L-a)}{2E_1I_1} + \frac{M_2^2(L-a)}{2E_2I_2} \\ &= \frac{B(L-a)(E_1h_1^3 + E_2h_2^3)}{72\rho^2(h_1+h_2)^2}\left[h_1^2 + h_2^2 + 3(h_1+h_2)^2 + \frac{E_1h_1^3}{E_2h_2} + \frac{E_2h_2^3}{E_1h_1}\right], \end{aligned} \tag{A3}$$

where L is the distance between the wedge loading points and the end of the specimen as shown in Fig. A1. G_T is eventually found to be

$$G_T = -\frac{1}{B}\frac{\partial U_b}{\partial a} = \frac{E_1h_1^3 + E_2h_2^3}{72\rho^2(h_1+h_2)^2}\left[h_1^2 + h_2^2 + 3(h_1+h_2)^2 + \frac{E_1h_1^3}{E_2h_2} + \frac{E_2h_2^3}{E_1h_1}\right]. \tag{A4}$$

An interesting feature from this result is that G_T is only a function of materials constants and the radius of curvature of the two beams, which can be measured experimentally.

For the present system, the measured radius of curvature of the ADCB specimen ranges from 0.8 to 2.0 m, depending on the thickness ratio and surface pretreatment, and the calculated G_T ranges from 10 to 70 J/m^2. The average radius of curvature for the selected thickness ratio in this study is about 1.2 m, corresponding to a G_T value of 26 J/m^2. This is within the experimental error of the dry strength (G_{dry}) measurements and, thus, can be neglected. For wet strength measurement, however, G_T could account for 8–20% of G_{wet}. Fortunately, G_T does not depend on crack length so the values were almost the same for the same series of samples. Therefore, the G_T values were not reported.